The Astrophysical Journal, 702:63–74, 2009 September 1 doi:10.1088/0004-637X/702/1/63

MOLECULAR GAS DISK STRUCTURES AROUND ACTIVE GALACTIC NUCLEI

Keiichi Wada[1,4], Padeli P. Papadopoulos[2], and Marco Spaans[3]
[1] National Astronomical Observatory of Japan, Mitaka, Tokyo 181-8588, Japan; wada@cfca.jp
[2] Argelander-Institüt für Astronomie, Auf dem Hügel 71, D-53121, Germany; padeli@astro.uni-bonn.de
[3] Kapteyn Institute, Netherlands; spaans@astro.rug.nl
Received 2009 January 13; accepted 2009 June 30; published 2009 August 7

ABSTRACT

We present new high-resolution numerical simulations of the interstellar medium (ISM) in a central $R \leqslant 32$ parsecs region around a supermassive black hole ($1.3 \times 10^7\ M_\odot$) at a galactic center. Three-dimensional hydrodynamic modeling of the ISM (Wada & Norman 2002) with the nuclear starburst now includes tracking of the formation of molecular hydrogen (H_2) out of the neutral hydrogen phase as a function of the evolving ambient ISM conditions with a finer spatial resolution (0.125 pc). In a quasi-equilibrium state, mass fraction of H_2 is about 0.4 (total H_2 mass is $\simeq 1.5 \times 10^6\ M_\odot$) of the total gas mass for the uniform far ultra-violet (FUV) with $G_0 = 10$ in Habing unit. As shown in the previous model, the gas forms an inhomogeneous disk, whose scale height becomes larger in the outer region. H_2 forms a thin nuclear disk in the inner $\simeq$5 pc, which is surrounded by molecular clouds swelled up toward $h \lesssim 10$ pc. The velocity field of the disk is highly turbulent in the torus region, whose velocity dispersion is $\simeq$20 km s^{-1} on average. Average supernova (SN) rate of $\simeq 5 \times 10^{-5}$ yr^{-1} is large enough to energize these structures. Gas column densities toward the nucleus larger than 10^{22} cm^{-2} are observed if the viewing angle is smaller than $\theta_v \simeq 50^\circ$ from the edge-on. However, the column densities are distributed over almost two orders of magnitude around the average for any given viewing angle due to the clumpy nature of the torus. For a stronger FUV ($G_0 = 100$), the total H_2 mass in an equilibrium is only slightly smaller ($\simeq$0.35), a testimony to the strong self-shielding nature of H_2, and the molecular gas is somewhat more concentrated in a midplane. Other properties of the ISM are not very sensitive either to the FUV intensity or the SN rate. Finally, the morphology and kinematics of the circum nuclear molecular gas disks emerging from our models are similar to that revealed by recent near infrared observations using VLTI/Keck.

Key words: galaxies: Seyfert – galaxies: starburst – ISM: molecules – ISM: structure – methods: numerical

Online-only material: color figures

1. INTRODUCTION

Optically thick molecular materials have been postulated to unify various observational properties of active galactic nuclei (AGNs), especially the two major categories of the AGN, namely type 1 and type 2 (Antonucci 1993). It is often assumed that the obscuration is caused by dusty molecular gas around a supermassive black hole (SMBH), whose geometry is schematically described as a doughnut-like "torus" (e.g., Urry & Padovani 1995). Its spatial extent and structures are deduced from comparison between observations in near/far infrared and theoretical spectral energy distributions (SED) based on radiative transfer calculations (e.g., Fritz et al. 2006; Elitzur 2008). Detailed three-dimensional radiative transfer calculations suggest that the torus should not be uniform but clumpy (Schartmann et al. 2008). In these model calculations, structures of the torus and its internal clumps are freely assumed, and then are tested in comparison with the observed SEDs. For example, the inner and outer edges of the torus are assumed typically as a subparsec and several tens of parsecs, respectively, and several hundred dense internal clumps are also assumed. It was then suggested that SEDs with the silicate absorption feature at 10 μm are mostly affected by the inner pc region of the torus (Schartmann et al. 2008).

Recently the dusty gas in the circum nuclear region are directly observed in some nearby Seyfert galaxies using interferometric mid-infrared observations. The prototypical type 2 Seyfert NGC 1068 harbors a warm (320 K) dust in a structure, 3.4 pc in diameter and 2.1 pc in thickness (Jaffe et al. 2004). VLTI/MIDI survey of nearby AGNs with various types recently revealed that in the most objects AGN-heated dust is spatially compact (∼a few pc)(Poncelet et al. 2006; Tristram et al. 2007; Meisenheimer et al. 2007; Tristram et al. 2009). These observations showed a structure of the hot dust and gas in a central few parsecs region, which may not necessarily encompass the whole structure of the molecular gas in the central region. Colder molecular gas probably extends further out, in $R \sim 10$ pc to subkiloparsec regions. Indeed using ^{12}CO(2 − 1) line observations, Hsieh et al. (2008) revealed that the molecular gas in Seyfert 1 galaxy, NGC 1097, is concentrated in $R \sim$175 pc, with an average density of the molecular hydrogen of $n_{H_2} \sim 3 \times 10^4$ cm^{-3}. Central concentrations of high-density gas around AGNs have been found via the observations of molecular lines with high-critical densities such as HCN$J = 1 - 0$ ($n_{crit} = 2.3 \times 10^5$ cm^{-3}) (e.g., Kohno et al. 2003).

If such quantities of circum nuclear molecular gas are present, then star formation is naturally expected. In fact, there are many lines of evidence of circum nuclear starbursts in various types of AGNs and quasars (Cid Fernandes et al. 2004; Imanishi & Wada 2004; Davies et al. 2007; Maiolino et al. 2007; Riffel et al. 2007; Watabe et al. 2008; Chen et al. 2009). Hicks et al. (2009) recently revealed structures of the interstellar medium (ISM) in local AGNs traced by $S(1)\nu = 1 - 0$ line of molecular hydrogen at 2.1 μm using VLT/SINFONI. They found that the ISM whose scale is $r \sim 30$ pc forms a rotating disk with a high-velocity dispersion, and correlated with the star formation rate. The average gas mass is estimated to $\sim 10^7\ M_\odot$, with a

[4] Also at Department of Astronomical Science, The Graduate University for Advanced Studies, Osawa 2-21-1, Mitaka, Tokyo 181-8588, Japan.

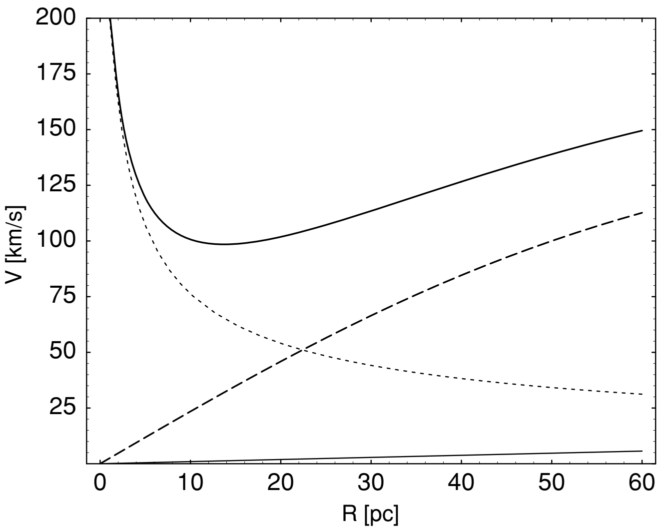

Figure 1. Assumed rotation curve (thick solid line) and contribution from each component of the external potential. Thick dashed line ($a_1 = 100$ pc, $v_1 = 147$ km s^{-1}) and thin line ($a_2 = 2500$ pc, $v_2 = 147$ km s^{-1}) are from $\Phi_{\rm ext}$, and thick dotted line is from $\Phi_{\rm BH}$ with $M_{\rm BH} = 1.3 \times 10^7\ M_\odot$.

column density of $N_{\rm H} > 2 \times 10^{22}$ cm^{-2}. They suggest that star formation occurs within a clumpy molecular gas phase. It has been observationally suggested that the starburst phenomena is linked with the nuclear activities (Watabe et al. 2008; Chen et al. 2009), and this connection was analytically studied based on a clumpy, turbulent accretion disk (Vollmer & Beckert 2003; Vollmer et al. 2004; Kawakatu & Wada 2008; Vollmer et al. 2008; Collin & Zahn 2008).

In order to construct physical models of the obscuring material around a SMBH, influenced also by concomitant star formation, three-dimensional radiative magnetohydrodynamic calculations with a sufficiently high resolution and a fairly large dynamic range (e.g., from 100 Schwarzschild radii to 100 pc) are ultimately necessary. However, until now, there are a few hydrodynamic studies in the central tens pc (Wada & Norman 2002; Wada & Tomisaka 2005; Yamada et al. 2007; Schartmann et al. 2009). Wada & Norman (2002) (hereafter WN02) investigated evolution of the ISM in the inner 100 pc region around a $10^8\ M_\odot$ SMBH using three-dimensional Euler-grid hydrodynamic simulations, taking into account self-gravity of the gas, radiative cooling and heating due to supernovae (SNe). They found that a clumpy torus-like structure is naturally reproduced on a scale of tens pc around a SMBH. The internal density and temperature are highly inhomogeneous, and the velocity field is turbulent, but the global geometry, i.e., a flared thick disk, is quasi-stable, implying that energy input from SNe is balanced with turbulent dissipation. They suggested that AGNs could be obscured by the surrounding interstellar material. These results support observational findings that some AGNs are obscured by nuclear starbursts (Levenson et al. 2001, 2007; Ballantyne 2008, and references therein). However, the models in WN02 are not necessarily applicable to all circum nuclear regions with active star formation, because (1) the assumed supernova (SN) rate is extremely high ($\sim 10^{-4}$ yr^{-1} pc^{-2}), which would be appropriate only for intense starburst, like ultraluminous infrared galaxies, but not to standard circum nuclear starbursts (e.g., Hicks et al. 2009), and (2) the cold, dense gas in their simulations does not necessary represent the dusty molecular gas phase around an AGN, because H_2 formation and its radiative destruction by far ultraviolet radiation (FUV) from massive stars and collisional destruction are not included. As a result, the radiative cooling in WN02 is not consistent with the chemical abundances in the low temperature medium.

Including the molecular gas in numerical models will eventually yield a much richer interface with current and future observations. This is because unlike the dust continuum, the effectively optically thin molecular line emission (even large line-center optical depths allow full view of turbulent media), is a direct probe of the velocity fields and thus of the gaseous disk dynamics, unobscured by the concomitant dust. The upcoming commissioning of ALMA will drastically enlarge such an interface by enabling the imaging of a whole suite of molecular lines probing different density and temperature regimes at high-angular resolution. However, from the results of WN02 it is still unclear how the various density regimes of the H_2 gas would be distributed in the circum nuclear region, and what would influence its structures. We hereby extend the three-dimensional hydrodynamic simulations of WN02 to explicitly track the evolution of the H_2 phase in the central $64^2 \times 32$ pc region, and its interplay with the HI phase, with a 0.125 pc resolution (cf. 0.25 pc in WN02). We also vary the strength of the uniform FUV field and the SN rate in order to examine their effect on the structures of molecular gas.

2. NUMERICAL METHOD AND MODELS

2.1. Numerical Methods

We use a numerical scheme based on Eulerian hydrodynamics with a uniform grid, which is the same as those described in Wada & Norman (2001); Wada (2001). Here, we briefly summarize them. We solve the following equations numerically to simulate the three-dimensional evolution of a rotating gas disk in a fixed spherical gravitational potential

$$\partial\rho/\partial t + \nabla\cdot(\rho v) = 0, \quad (1)$$

$$\partial v/\partial t + (v\cdot\nabla)v + \nabla p/\rho = -\nabla\Phi_{\rm ext} - \nabla\Phi_{\rm BH} - \nabla\Phi_{\rm sg}, \quad (2)$$

$$\partial E/\partial t + \nabla\cdot[(\rho E + p)v]/\rho = \Gamma_{\rm UV}(G_0) + \Gamma_{\rm SN} - \rho\Lambda(T_g, f_{\rm H_2}, G_0), \quad (3)$$

$$\nabla^2\Phi_{\rm sg} = 4\pi G\rho, \quad (4)$$

where, the specific total energy $E \equiv |v|^2/2 + p/(\gamma-1)\rho$, with $\gamma = 5/3$. We assume a time-independent external potential $\Phi_{\rm ext} \equiv -(27/4)^{1/2}[v_1^2/(r^2+a_1^2)^{1/2} + v_2^2/(r^2+a_2^2)^{1/2}]$, where $a_1 = 100$ pc, $a_2 = 2.5$ kpc, $v_1 = 147$ km s^{-1}, $v_2 = 147$ km s^{-1}, and $\Phi_{\rm BH} \equiv -GM_{\rm BH}/(r^2+b^2)^{1/2}$, where $M_{\rm BH} = 1.3\times 10^7\ M_\odot$ and $b = 1$ pc. See Figure 1 for the rotation curve based on the external potentials $\Phi_{\rm ext}$ and $\Phi_{\rm BH}$. Observationally, it is hard to determine exact rotation curves in the central 100 pc region of external galaxies, the adopted mass distribution with a core radius of 100 pc is roughly consistent with the rotation curves around nearby Seyfert nuclei observed by VLTI/Keck (Hicks et al. 2009). CO(1–0) observations of the central region of nearby spiral galaxies also show that their rotation curves are steep in the central part, suggesting central massive components (Sofue et al. 1999). This could correspond to the stellar cores found by *HST*/NICMOS in nearby galaxies (Carollo et al. 2002). The potential caused by the black hole (BH) is smoothed inside $r \sim 1$ pc by introducing a "softening" parameter b, in order to avoid too small time steps around the BH. This softening does not change the rotation curve in the range shown in Figure 1, but we should not rely on the gas dynamics and structures at $r < 1$ pc. In the central grid cells at $r < 0.25$ pc, physical quantities stay constant to represent a sink cell.

The hydrodynamic part of the basic equations is solved by AUSM (Advection Upstream Splitting Method) (Liou & Steffen 1993; Wada & Norman 2001). We use $512^2 \times 256$ grid points in high-resolution models and $256^2 \times 128$ grid points in low resolution models to investigate long-term evolution with different parameters.[5] Cartesian grid points cover a $64^2 \times 32$ pc^3 region around the galactic center (i.e., the spatial resolution is 0.125 pc in the high-resolution runs and 0.25 pc for the low resolution runs). The Poission equation, Equation (4) is solved to calculate the self-gravity of the gas using the Fast Fourier Transform (FFT) and the convolution method, where $1024^2 \times 512$ grid points and a periodic Green's function is used to calculate the potential of an isolated system (Hockney & Eastwood 1981).

An essential progress in the present calculations compared to WN02 is that we now solve nonequilibrium chemistry of hydrogen molecules along with the hydrodynamics. Formation of H_2 on dust and its radiative and collisional destruction are explicitly tracked, therefore we can deduce the distribution of H_2 in the central tens pc region. See details in Appendix A.

In the energy equation (Equation (3)), we use a cooling function based on a radiative transfer model of photodissociation regions (PDRs; Meijerink & Spaans 2005), $\Lambda(T_g, f_{H_2}, G_0)$ (20 K $\leqslant T_g \leqslant 10^8$ K) assuming solar metallicity, which is a function of the molecular gas fraction f_{H2} and intensity of FUV, G_0 (see Appendix B for the detail). The radiative cooling rate below $\simeq 10^4$ K is self-consistently modified depending on f_{H_2}, which is determined in each grid cell. We adopt heating due to the photoelectric effect, Γ_{UV} and energy feedback from type II SNe (see below), Γ_{SN}. We assume a uniform UV radiation field, whose strength is an important parameter in the model, represented by the Habing unit (G_0), the incident FUV field normalized to the local interstellar value.

2.2. Initial Conditions and Model Parameters

The initial condition is an axisymmetric and rotationally supported thin disk with a uniform density profile (thickness is 2.5 pc) and a total gas mass of $M_g = 6 \times 10^6 M_\odot$. Since we allow outflows from the computational boundaries, the total gas mass decreases during the evolution, and it settles to $\simeq 5 \times 10^6 M_\odot$ at a quasi-equilibrium state. Random density fluctuations, which are less than 1% of the unperturbed values, are added to the initial gas disk. A uniform disk with $\rho = 1.22 \times 10^3 M_\odot$ pc^{-3} at $t = 0$ is evolved for $t = 1.4$ Myr (the rotational period at $R = 10$ pc is about 0.2 Myr) using $256^2 \times 128$ grid points (i.e., spatial resolution is 0.25 pc), then it continues to higher resolution runs with $512^2 \times 256$ grid points. The system settles into a quasi-equilibrium state, where the total molecular gas mass is nearly constant, after $t \sim 3.5$ Myr (see Section 3.2 and Figure 6).

Since the current integration time is short ($\simeq$5 Myr) due to a limitation of our computational resources, instead of tracking the whole life of massive stars, here we assume that supernova (SN) explosions occur at random positions with a constant rate in the region confined by $r \leqslant 26$ pc and $|z| \leqslant 2$ pc. Here, we effectively assumed that massive, cold molecular gases from which stars formed are not distributed spherically, but they are rather concentrated in a disk with a small scale height. Therefore, we expect that SN explosions mostly occur near the disk plane.

The average SN rate is one of the free parameters in the present study. Observationally, there is a large ambiguity in the star forming activities around AGNs. the SFR around AGNs was suggested to several tens $M_\odot$ yr^{-1} kpc^{-2} (Davies et al. 2007). For the Salpeter initial mass function (IMF) and stellar mass rage of 0.1–125 $M_\odot$, type II SN rate is $\simeq$0.007 SFR, and a corresponding SN rate per unit area would be $\sim 10^{-7}$ yr^{-1} pc^{-2}. For the circum nuclear disk of $r = 26$ pc in the present model, this rate suggest that $\simeq 3 \times 10^{-4}$ yr^{-1}. On the other hand, using the scaling relation on the SFR in galactic disks and in starbursts (Kennicutt 1998), the initial gas density in the present model yields 4×10^{-4} yr^{-1}. We here change the SN rate from 5.4 to 540 $\times 10^{-5}$ yr. For each type II SN explosion, the energy of 10^{51} erg as thermal energy and gas mass 8 $M_\odot$ are instantaneously injected into a single cell. Note that since we set a maximum temperature of 10^8 K, not all the injected thermal energy is used to create blast waves. Three-dimensional evolution of blast waves caused by SNe in an inhomogeneous and nonstationary medium with global rotation are followed explicitly, taking into account the radiative cooling, which makes the evolution of the supernova remnants depending on the local gas density distribution around the SNe.

We here assume a spatially uniform FUV field with $G_0 =$ 10 and 100. For a PDR surrounding an H II region, $G_0 \simeq 2 \times 10^2 (L/10^4 L_\odot)(r/1 \text{ pc})^{-2}$ (e.g., Tielens 2005, p. 319). For the SFR $10^{-5} M_\odot$ yr^{-1} pc^{-2}, which is a typical rate in starburst galaxies, the luminosity of massive stars formed for 10^7 yr that contribute to the FUV field is roughly $10^4 L_\odot$ pc^{-2}. If we assume that the massive stars are embedded in the uniform gas disk with $n \sim 10^4$ cm^{-3}, contribution from local ($\lesssim$a few pc) stars is important. Then the average local FUV field in a grid cell of 0.1 pc would be $G_0 \sim 200$. On the other hand, an AGN would have a negligible effect on the FUV field in most of the regions, because the average column density through the initial thin disk is $\gtrsim 10^{23}$ cm^{-2} for $r \gtrsim 2$ pc. However, as we will see in Section 3, the star-forming disk in a quasi-equilibrium state is highly inhomogeneous, especially in the outer region ($r \gtrsim 5$ pc). Therefore, G_0 could be several 10^3 for the low column density regions ($N \lesssim 10^{22}$ cm^{-2}) at $r \sim 10$ pc from a typical AGN with luminosity $L = 10^{44}$ erg s^{-1}. In reality, both the density field and distribution of massive stars are not uniform, and G_0 should have a large dispersion with some radial dependence. Effect of the nonuniform radiation field will be an important subject to solve by three-dimensional radiative transfer calculations in the future.

Beside the FUV, the X-ray radiation from the AGN would be important for the thermal and chemical structures of the ISM around an AGN (Maloney et al. 1996; Meijerink et al. 2007). This will be discussed in Section 5.

Model parameters are summarized in Table 1. For simplicity, we here assume that the FUV intensity and SN rate are independent free parameters. In reality, those quantities are tied to the ambient SFR density, which in turn is regulated by the H_2 gas density since stars always form out of the H_2 gas. It is therefore expected that FUV, SN rate, and H_2 gas mass fraction evolve in a highly coupled manner, leading perhaps toward a self-regulating, quasi-stationary state. This important issue can only be explored if a SF-regulating H_2 gas distribution

[5] In the high-resolution models, a calculation for 4.5 Myr requires about 180 CPU hours using 16 CPUs of NEC SX-9 whose peak performance is about 1.6 TFlops.

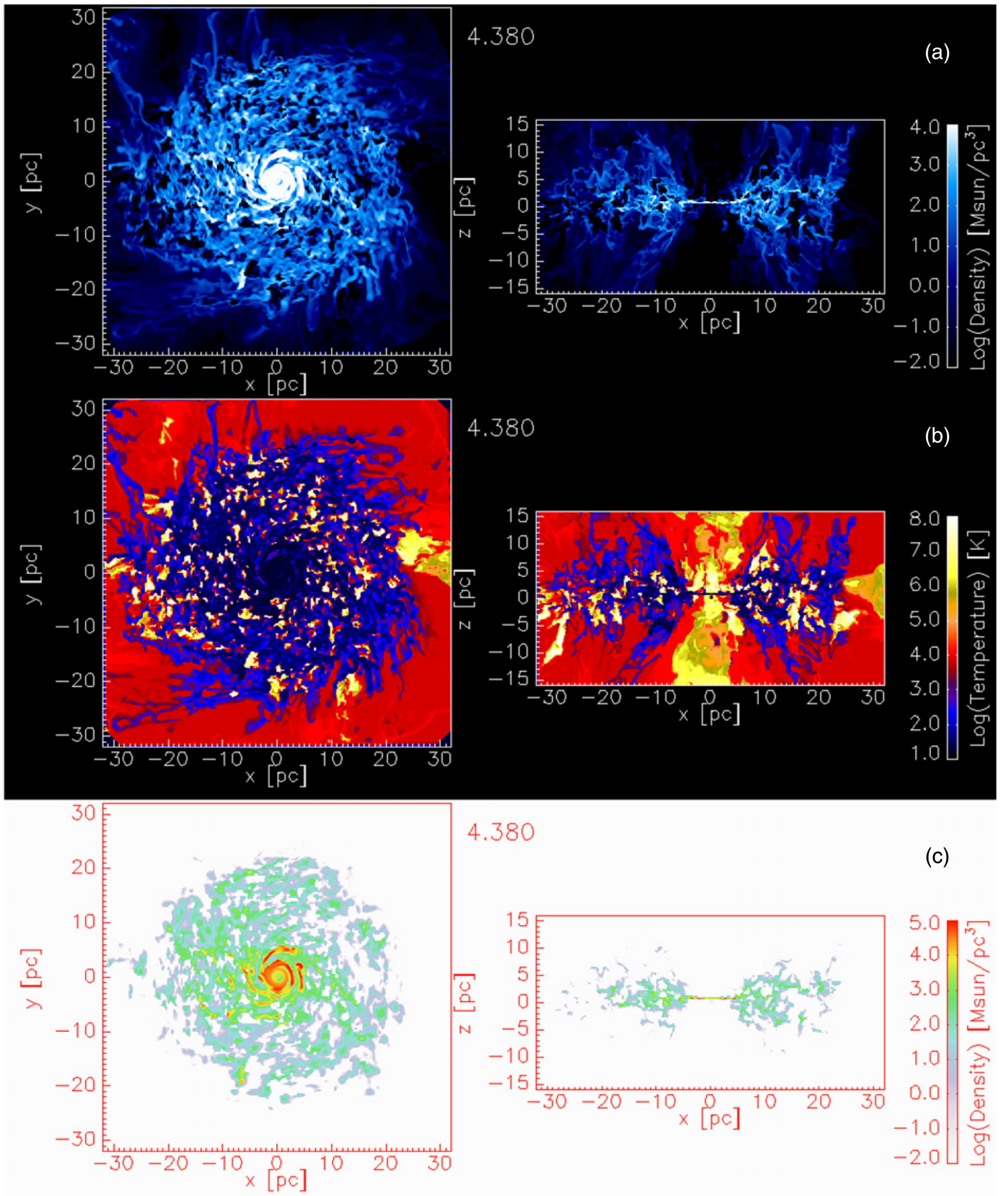

Figure 2. Cross sections (a) gas density [$M_\odot$ pc^{-3}], (b) temperature [K] and (c) H_2 density [$M_\odot$ pc^{-3}] on x–y and x–z planes of model H10a ($t = 4.38$ Myr). (A color version of this figure is available in the online journal.)

Table 1
Model Parameters

Model	G_0	Δ [pc]	SN rate [10^{-5} yr^{-1}]
H10a	10	0.125	5.4
L10a	10	0.25	5.4
H100a	100	0.125	5.4
L100a	100	0.25	5.4
L100b	100	0.25	54.0
L100b*	100	0.25	54.0
L100c	100	0.25	540.0

Notes. "H/L" represents "High/Low" resolution (Δ, size of a numerical grid cell), "100/10" represents intensity of far ultraviolet radiation in the Habing unit (G_0), and suffix "a-c" represent the average supernova rate (SN rate). L100b* is the same as L100b, but energy from supernovae is injected in a larger scale height, i.e., $|z| \leqslant 10$ pc.

is included in the ISM+stars model, and we intend to do so in a future paper.

3. RESULTS

3.1. Structures of a Fiducial Model

In a quasi-steady state ($t \gtrsim 3.5$ Myr), as reported by WN02, the gas forms a highly inhomogeneous, flared disk, as seen in Figure 2, which shows gas density, temperature and molecular hydrogen density in model H100a at $t = 4.38$ Myr. The temperature map shows that cold ($T_g \lesssim 100$ K) gas is mainly distributed in the high-density regions. In the central funnel-like cavity, the temperature of the gas is hot ($T_g \gtrsim 10^6$ K). Hot gases are also patchily distributed in the cold, flared disk. Typical size of these hot cavities is a few parsecs. A large fraction of the volume is occupied by warm gas ($T_g \simeq 8000$ K). As expected, distribution of H_2 roughly follows the cold, dense gas, and therefore it forms a high-density circum nuclear disk whose radius is about 5 pc, surrounded by a porous torus which extends to ∼5–10 pc above the disk plane.

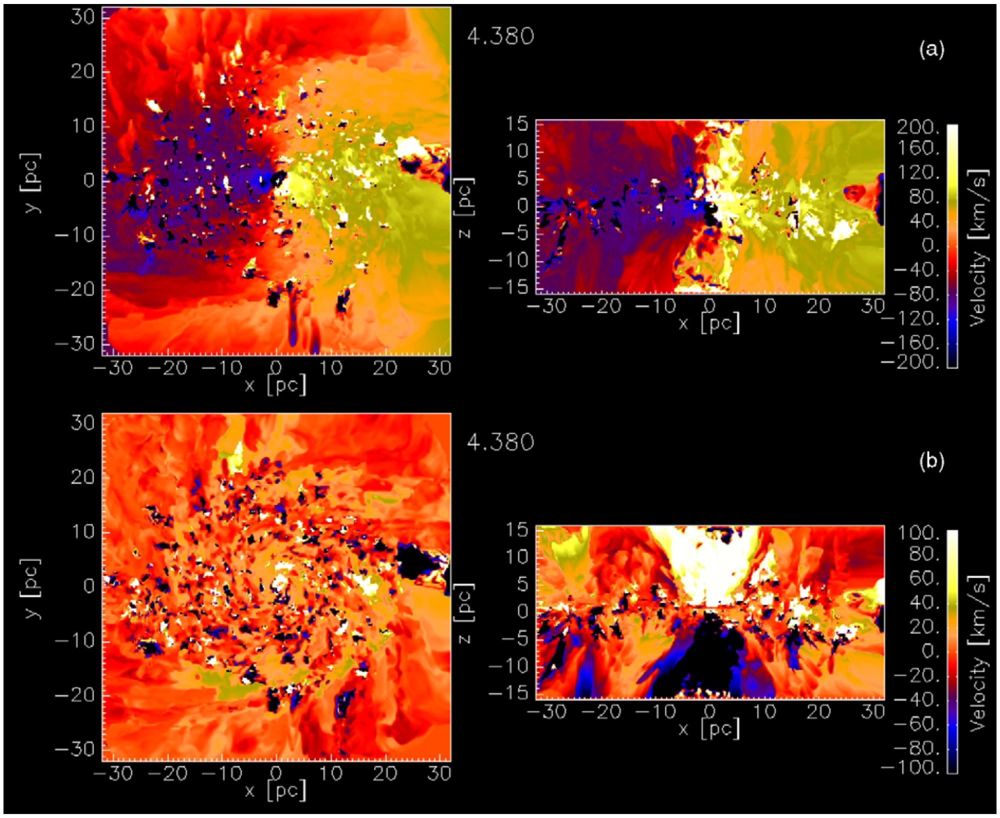

Figure 3. Same as Figure 2, but for velocity fields of the gas: (a) velocity for y-direction, and (b) velocity for z-direction.
(A color version of this figure is available in the online journal.)

Figure 3 shows velocity fields of two components (v_y and v_z) at the same snapshot of Figure 2. The torus shows a global rotation, but there are also large internal random motions. This complicated velocity field is naturally expected in an inhomogeneous, self-gravitating disk (Wada et al. 2002), but the vertical motions are mainly enhanced by energy input from SNe (see also Figure 8). The vertical velocity field also shows a bipolar outflow in the central funnel, which is mostly warm and hot gases as seen in Figure 2(b).

In Figures 4(a) and 4(b), we plot total column density ($N_{\rm g}$) and H_2 column density ($N_{\rm H_2}$) toward the galactic center as a function of the viewing angle in model H10a. It clearly shows that the total gas and H_2 column densities are both largest at $\theta_v \simeq 0$ (i.e., edge-on), and the average column density decreases on average toward the pole-on view as expected. We should note, however that the scatter around the average is 2 orders of magnitude or more for any viewing angles, which is comparable to the change of the average value between $\theta_v = 0^\circ$ and $\pm 90^\circ$. Figure 4(b) shows that H_2 is distributed similarly, but it is more concentrated near the disk plane. The scatter of $N_{\rm H_2}$ is more significant than that in $N_{\rm g}$ especially for $\theta \gtrsim 50^\circ$, reflecting that H_2 gas is highly inhomogeneous and more sparsely distributed in larger latitudes.

3.2. Dependence of Model Parameters

Figure 5 shows density distributions of models with two resolutions, H100a ($\Delta = 0.125$ pc) and L100a ($\Delta = 0.25$ pc) at $t = 4.02$ Myr. The inhomogeneous density fields and global morphology of the thick disk in the two models are qualitatively similar, but clumpy structures are finer in the high-resolution model, H100a than in L100a. In Figure 6, evolution of molecular gas fractions, $f_{\rm H_2} \equiv M_{\rm H_2}/M_{\rm total}$, in five models is shown. The molecular gas fraction in H10a rapidly decreases from $f_{\rm H_2} \simeq 0.5$ to $\simeq 0.32$ in the first Myr, then it increases and slightly oscillates around $f_{\rm H_2} \simeq 0.4$. The model with 10 times stronger FUV (H100a) shows a similar time evolution, with $f_{\rm H_2}$ only about 10% smaller than in model H10a. In order to see a longer term evolution, we restart calculations from a snapshot of the high-resolution data at $t = 2.5$ Myr with a lower resolution (i.e. 0.25 pc).[6] The low resolution run (L10a) shows rapid decrease of $f_{\rm H2}$ in the first $\sim$0.2 Myr, reverses to an increase at $t \sim 2.7$ Myr, and then settles around $f_{\rm H_2} \simeq 0.4$ after $t \sim 3.5$ Myr in L10a as in H10a. Molecular fraction of L100a in the quasi-equilibrium state is $f_{\rm H_2} \simeq 0.32$. These results suggest that for *a given SN rate and the FUV intensity there is an equilibrium H_2 fraction which does not significantly depend neither on the numerical resolution nor on the initial state.* For stronger FUV fields, H_2 is less abundant, but this is not very sensitive to G_0 because of the effective H_2 self-shielding against far-UV dissociation. In the low resolution runs, we change energy input rate due to the SN rate by a factor of 100 (see Table 1). As seen in Figure 6, L100a and L100c show similar evolution, but the molecular fraction is only slightly smaller in the model with 100 times larger SN rate.

Figure 7 shows column density distribution of H_2 in models H10a and H100a at $t = 3.47$ Myr. The dependence of $N_{\rm H_2}$ on the viewing angles are similar in the two models, but in H100a, H_2 more rapidly decreases toward high latitudes. This is naturally expected because H_2 is mainly formed in the dense regions, which are concentrated near the disk plane. Strong

[6] The computational time in the high-resolution run is about 16 times longer than that in the low resolution runs.

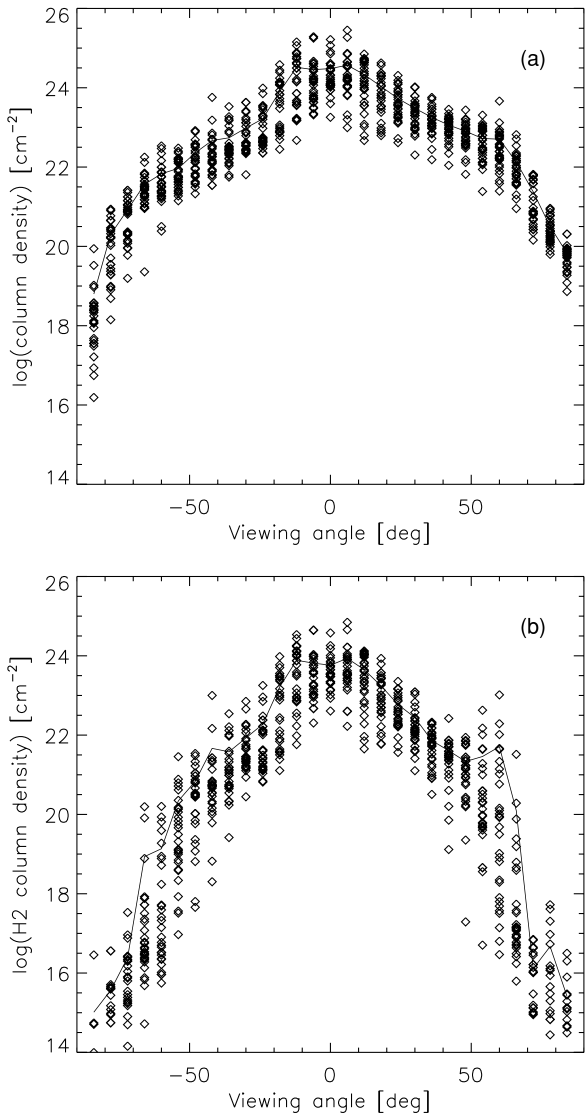

Figure 4. (a) Column density of the gas, N_g and column density of H_2, N_{H_2} as a function of the viewing angle in model H10a at $t = 4.38$ Myr. The solid line represent an azimuthally averaged column density.

FUV can easily dissociate H_2 in the relatively diffuse regions at high latitudes. However, those differences in the two models are not significant. Even in the strong FUV model, H_2 is inhomogeneously distributed in the central tens pc.

We compare vertical velocity dispersion of the gas below $T_g = 2000$ K in three models (L100a, L100b, and L100c) with different SN rates in Figure 8. It shows that velocity dispersion tends to increase with higher SN rate. However its dependence in the torus region is less than factor of 2 when the SN rate is 100 times larger. The effect is more significant in the inner region, where there is a bipolar outflow from the central funnel (Figure 3).

4. DISCUSSION

4.1. Comparison with Observations

Hicks et al. (2009) recently revealed structures of the ISM in local AGNs traced by a $S(1)\, \nu = 1 - 0$ line of molecular hydrogen at 2.1 μm using the near-infrared field spectrograph SINFONI at ESO Very Large Telescope (VLT) and OSIRIS at Keck Observatory. They found that ISM with a radius of $r \sim 30$ pc forms a rotating disk with a high-velocity dispersion (several tens km s^{-1}), and suggested that star formation is concomitant with clumpy molecular gas. The average gas mass is estimated to $\sim 10^7\, M_\odot$, assuming a 10% mass fraction to the dynamical mass. The size, mass, and dynamics of these nuclear molecular gas disk around AGNs are very similar to what we found here. The turbulent-like velocity field revealed by their observations qualitatively resembles to those seen in our models (Figure 3). They also suggest a positive correlation between the velocity dispersion of the hot molecular gas and the SFR, which is consistent with our result (Figure 8), and it is reasonable if turbulent velocity is energized by SNe and balanced by gas dissipation (WN02). Although $\nu = 1 - 0S(1)$ is emitted from warm gas, it is expected from our simulations that the cold molecular gas have also similar random velocity field.

Hsieh et al. (2008) observed a Seyfert 1 galaxy, NGC 1097 using ^{12}CO($J = 2 - 1$) by the submillimeter array at angular resolution of $4''.1 \times 3''.1$ (290 pc × 220 pc), and deduced a total mass of molecular hydrogen of $M_{H_2} \simeq 6.5 \times 10^7\, M_\odot$, with column densities $N_{H_2,CO} \simeq 5.9 \times 10^{22}$ cm^{-2}, and $N_{H,CO} \simeq 1.2 \times 10^{23}$ cm^{-2}. They suggest a clumpy disk configuration to explain inconsistency between the large column density suggested by their observations and 2 orders of magnitude smaller column density ($N_{H,X} \simeq 1.3 \times 10^{21}$ cm^{-2}) suggested by X-ray observations (Terashima et al. 2002). If the nucleus of this galaxy surrounded by a torus consisted of high density, small gas clumps, it would be possible to observe the broad line region through gaps between the clumps. On the other hand, the H_2 column density represents an average one in the large beam size (~250 pc), which should be much larger than than the value suggested by X-ray observations. Could this be the case in the clumpy H_2 in our results? The ratio $N_{H_2,CO}/N_{H,X}$ is $\simeq$45 in NGC 1097. Among our models, model H10a, in which the moderate star-forming activity is assumed ($G_0 = 10$ and SN rate $= 5.4 \times 10^{-5}$ yr^{-1}), would be appropriate for comparison. If one supposes that the H_2 column density inferred from the CO line observations represents an average column density of all the molecular gas present in the central several tens parsecs ($\langle N_{H_2} \rangle$), and column density of H suggested by X-ray reflects the amount of material along the line of sight (its viewing angle is θ_v) for the nucleus ($N_H(\theta_v)$). In Figure 9, we plot $\langle N_{H_2} \rangle / N_H$ in model H10a at $t = 4.38$ Myr. It is clear that we have smaller chances to observe small N_H if the line of sight is closer to the edge-on. $\langle N_{H_2} \rangle / N_H \gtrsim 10$ can be achieved for $\theta_v \sim 50^\circ$ or larger. One should note again that the scatter of the ratio is significant for any given viewing angles, and it also depends on the structure of molecular gas around the nucleus. It is therefore hard to conclude at this moment on structures of the circumnuclear region of NGC 1097. Future observations of AGNs using CO or other lines with much higher resolutions, at least with a few pc beam, by for example ALMA are necessary.

Jaffe et al. (2004) observed the central region of NGC 1068 by the Very Large Telescope Interferometer (VLTI), and suggested a dusty "torus" of thickness 2.1 pc, diameter 3.4 pc, and temperature of $T_g = 320$ K. This could correspond to the central, relatively smooth molecular dense disk typically seen in our models (Figure 2). Due to the strong gravity and shear caused by the central BH, it is natural that molecular gas forms a thin, smooth disk in the central few pc. However, if the observed central disk of NGC 1068 is geometrically thick, a strong heating source, e.g., infrared radiation would be necessary (Pier & Krolik 1993; Krolik 2007). Tristram et al. (2007) suggested

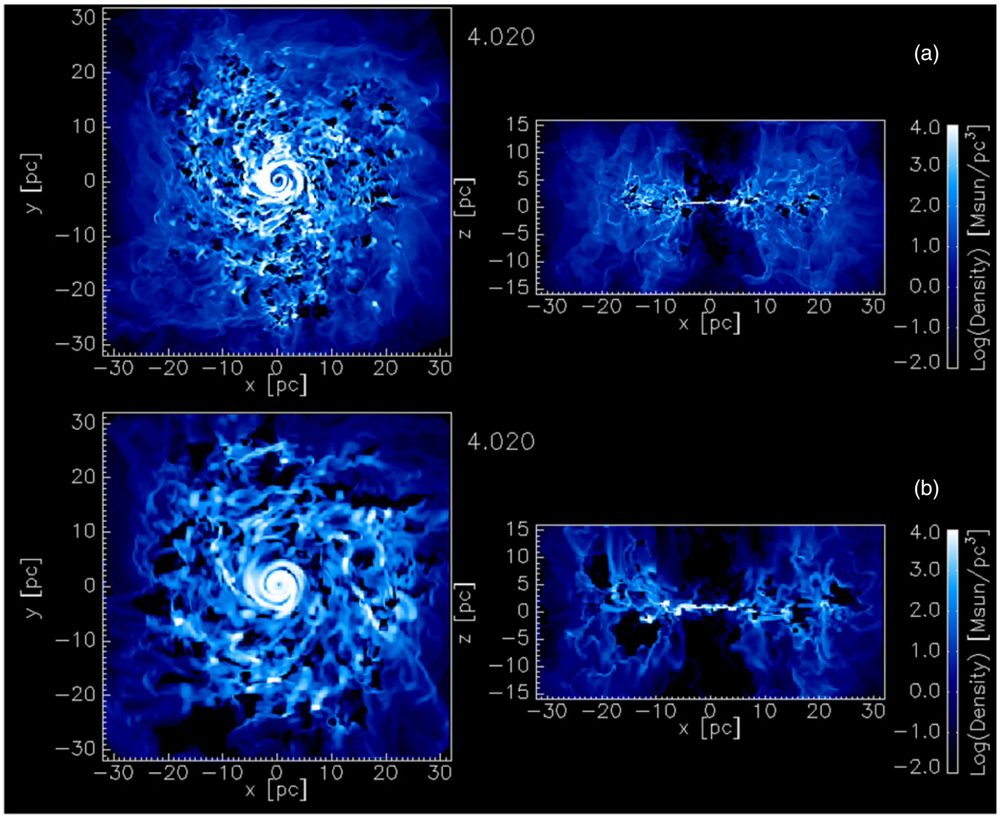

Figure 5. Density distributions on x–y and x–z planes (a) in a high-resolution model H100a and (b) in a low resolution model L100a at $t = 4.02$ Myr.
(A color version of this figure is available in the online journal.)

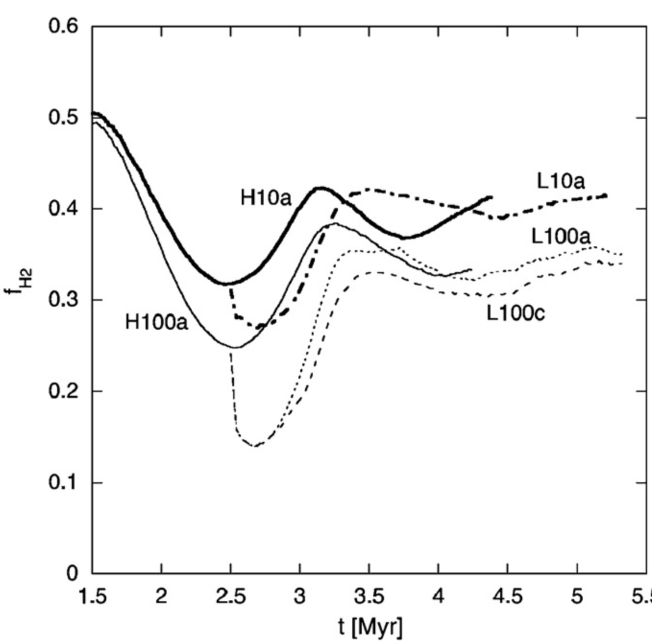

Figure 6. Evolution of molecular gas fraction f_{H2} in high-resolution models (H10a and H100a) and low resolution models (L10a, L100a and L100c) recalculating from the high-resolution runs at $t = 2.5$ Myr.

a clumpy torus plus a central thick disk model from mid-IR observations using VLTI of Circinus, which has a Seyfert 2 nucleus. Although the size is smaller (~2 pc), the geometry and structures suggested by their high-resolution observations (see a schematic picture in their Figure 9) is quite similar to the models presented here.

4.2. Effects of X-rays

The strong X-ray continuum emanating from the AGN could affect the chemical state of the ISM in the central region (Maloney et al. 1996; Meijerink et al. 2007). It is known that the chemical state of the X-ray Dissociated Region (XDR) is mainly determined by H_X/n, where H_X is a X-ray heating deposition rate and n is the number density of the gas (Maloney et al. 1996). Although we do not include the effect of X-ray from the nucleus, here we estimate its potential effect using one of our models. In Figure 10, we plot a fraction of H_2 and temperature as a function of H_X/n (erg cm^3 s^{-1}) at randomly selected points in the computational box. Here, we assume that the X-ray luminosity of the AGN is $L_X = 10^{44}$ erg s^{-1}. Although there is a large scatter, for $\log(H_X/n) \simeq -24$ or smaller, the molecule fraction increases significantly and the temperature in most regions is less than 100 K. At high-gas densities (~10^5 cm^{-3}), large (>0.1) H_2 fractions can be sustained for the range of H_X/n values, limiting the impact of XDR effects (Meijerink et al. 2007). This is partly because the free electrons associated with ionization processes help to form H_2 through the H^- route and also because H_2 formation scales with density squared. Still, for H_X/n significantly larger than 10^{-26}, gas is mostly atomic as expected (Maloney et al. 1996).

These results suggest that XDR chemistry may change distribution of H_2 around an AGN, if we explicitly include X-ray from the nucleus in the following sense. The H_2 abundance is indeed robust in a clumpy medium, but the XDR gas temperature should rise relative to the PDR case by a factor of ~5 for $\log H_X/n > -26$ (Meijerink et al. 2007). After all, X-ray ionization heating with for example $H_X/n \sim 10^{-25}$ erg cm^{-3} s^{-1}, is more efficient than photoelectric emission by dust grains,

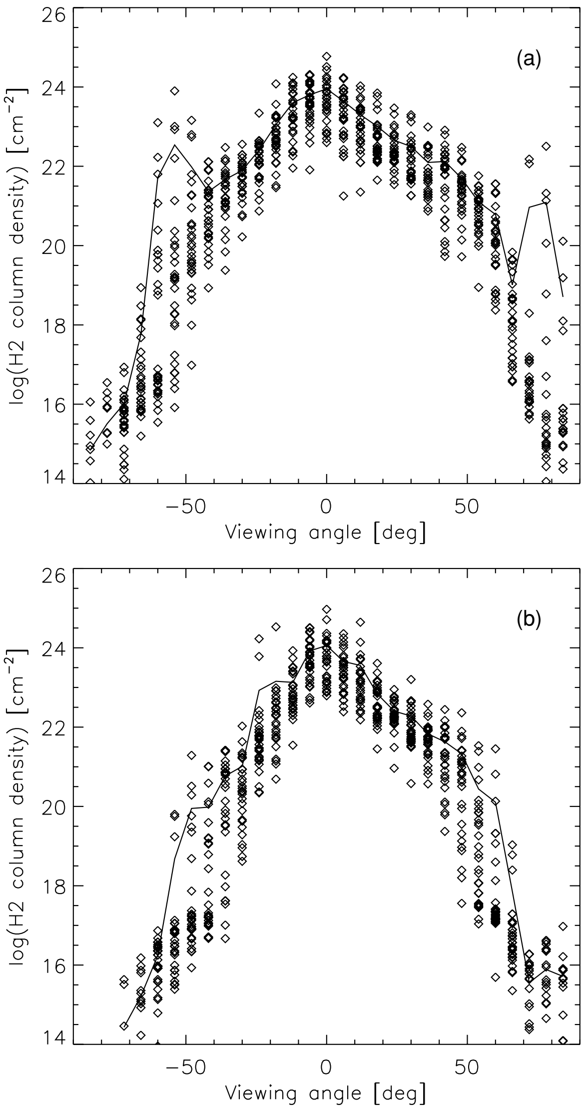

Figure 7. Column density of H_2 as a function of a viewing angle in H10a (Left: $G_0 = 10$) and H100a (Right: $G_0 = 100$) at $t = 3.47$ Myr. The solid line represent an average column density.

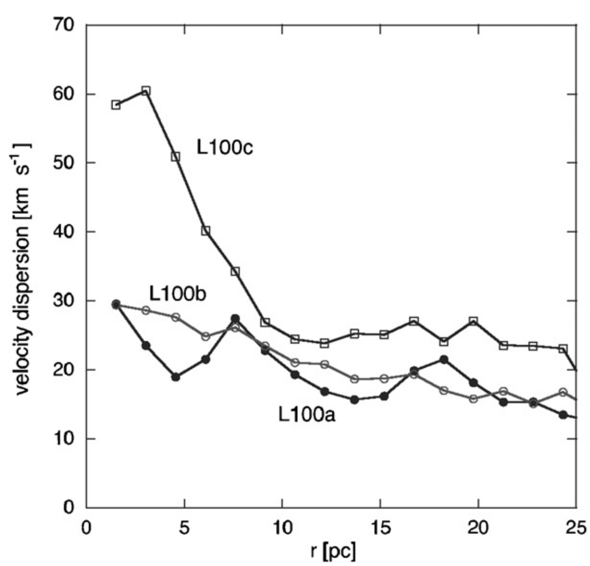

Figure 8. Azimuthally averaged velocity dispersion for z-direction as a function of radius in three models at $t = 5.32$ Myr. Supernova rates are 5.4×10^{-5} yr^{-1} (L100a), 5.4×10^{-4} yr^{-1} (L100b), and 5.4×10^{-3} yr^{-1} (L100c).

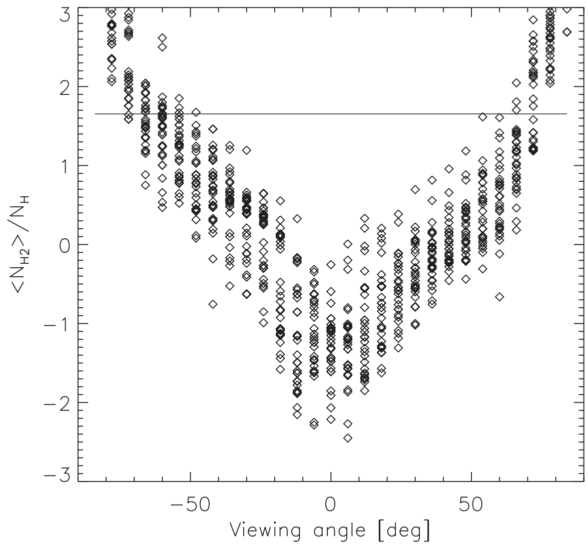

Figure 9. $\langle N_{H_2} \rangle / N_H$ as a function of the viewing angle for model H10a at $t = 4.38$ Myr. The horizontal line shows the ratio suggested by CO and X-ray observations in NGC 1097.

therefore H_2 gas would have higher temperatures. This leads to stronger emission in the pure rotational H_2 lines, such as $S(0)$, $S(1)$ at 28 μm, 17 μm. Similar considerations hold for CO (Spaans & Meijerink 2008). Shocks can heat as well, therefore observational data on line profile kinematics would be useful in the future.

4.3. A Self-regulated H_2 and the Star Formation Rate

In the present results, it is notable that although the assumed FUV and SN rate differ by orders of magnitude among the models, total molecular gas fraction settle between $f_{H_2} \simeq$ 0.3–0.4. There is a weak "negative" feedback of FUV and SNe on the star formation in the central region. This suggests that the molecular gas disk could survive around AGNs associated with a starburst. Since the negative feedback of FUV and SN rate on H_2 mass is "weak", it is also implied that if there is an episodic large mass inflow into the circum nuclear region, we expect a burst of star formation, because SFR depends on H_2 density. This could also affect the mass accretion rate toward the AGN via turbulent viscosity (Kawakatu & Wada 2008). To explore these mechanisms, the star formation, the radiative feedback from the AGN/stars affecting H_2 (the star formation fuel), and a coupled SN rate should be self-consistently followed (e.g., Wada 2008) for at least several tens Myr. These effects, along with incorporating the H_2-tracing CO molecule, will be investigated in a future paper.

4.4. Positions of Supernovae

Finally, effect of position of SNe on the gas density distribution is compared between L100b and L100b* (Figure 11). As explained in Section 2.2, we assumed that SN explosions occur at random positions with a constant rate in the region confined by $|z| \leqslant 2$ pc. This is justified by the results that H_2 is more concentrated in the disk plane. However, orbits of massive stars formed near the disk plane could have large inclination angles, as a result, energy from SNe could be released at higher latitudes. In model L100b*, SNe are assumed to be exploded in $|z| \leqslant 10$ pc (Figure 11(b)), but we do not see significant differences in the distribution of gas around AGNs.

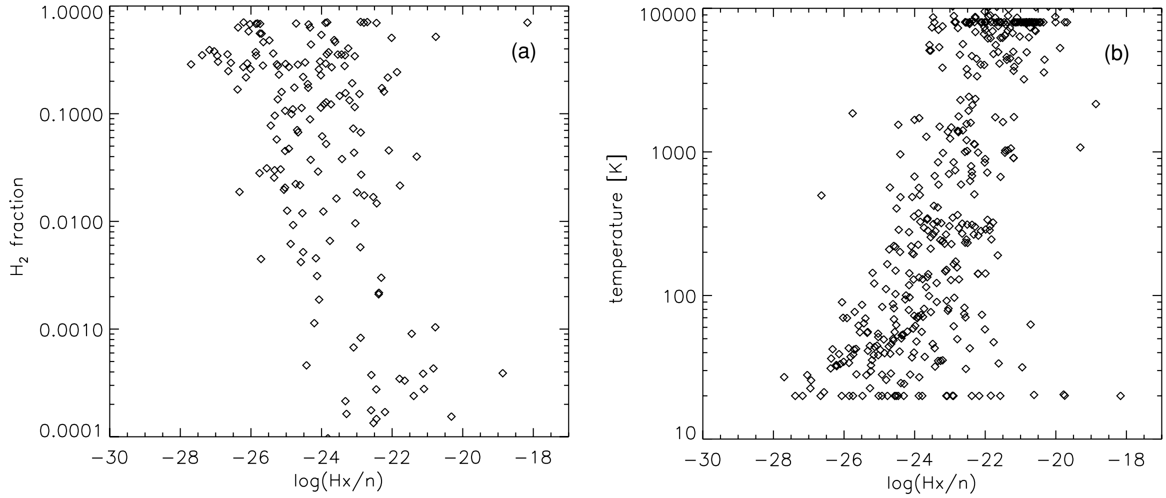

Figure 10. (a) H_2 fraction as a function of ratios of the X-ray heating deposition rate and gas density, H_X/n[erg cm^3 s^{-1}] for randomly selected 500 points in the computational box in model H10a at $t = 4.3$ Myr. (b) Same as (a), but for temperature. Note that H_2 fraction is zero in many selected points, because the hot and warm gas occupies a large volume, therefore the number of data points in the plot (a) is smaller than in (b).

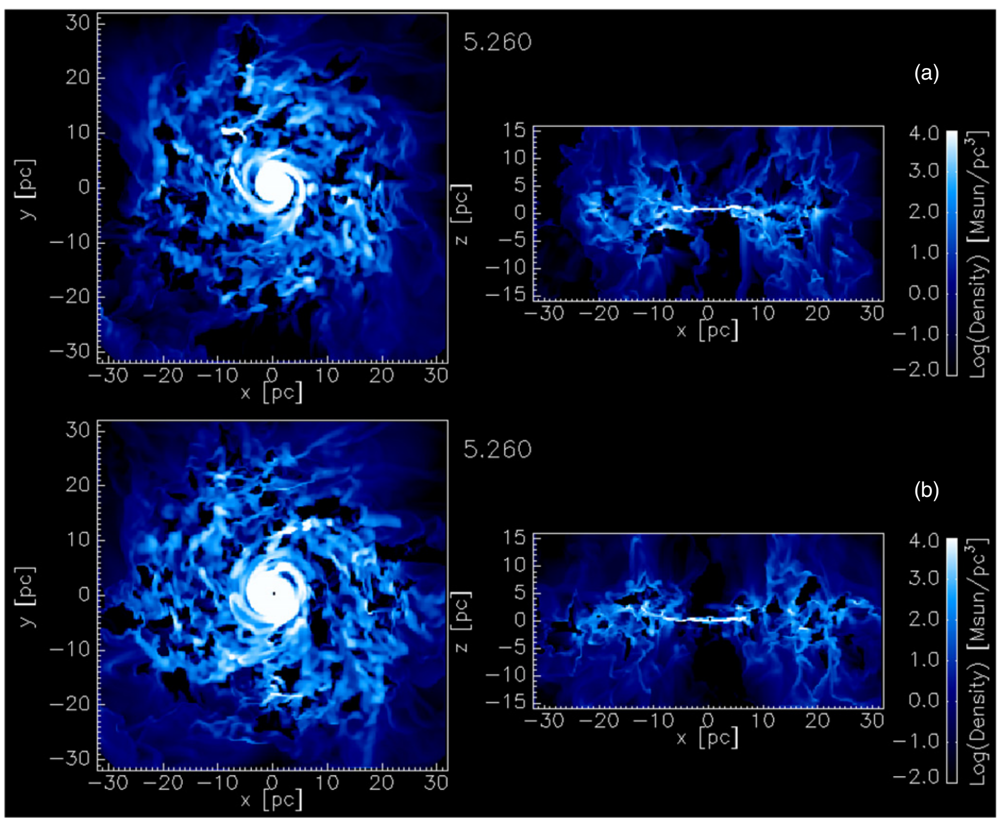

Figure 11. Density distributions in models with different positions of supernovae, $|z| \leqslant 2$ pc (L100b) and $|z| \leqslant 10$ pc (L100b*).
(A color version of this figure is available in the online journal.)

5. CONCLUSIONS

We present new high-resolution numerical simulations of the ISM in a central $R \leqslant 32$ pc region around a SMBH ($1.3 \times 10^7\ M_\odot$) at a galactic center. Three-dimensional hydrodynamic modeling of the ISM (Wada & Norman 2002) along with a concomitant starburst now includes tracking of the formation of molecular hydrogen (H_2) out of the neutral hydrogen phase as a function of the evolving ambient ISM conditions with a finer spatial resolution (0.125 pc). Radiative cooling rate is self-consistently changed depending on abundance of H_2 in each grid cell. In a quasi-equilibrium state, mass fraction of H_2 is about 0.4 (total H_2 mass is $\simeq 1.5 \times 10^6\ M_\odot$) of the total gas mass for the uniform FUV with $G_0 = 10$ in Habing unit. As shown in the previous model, the gas forms an inhomogeneous disk, whose scale height becomes larger in the outer region. H_2 forms a thin disk in the inner $\simeq 5$ pc, and it is clumpy and swelled up toward $h \simeq 10$ pc. The velocity field of the disk is highly turbulent in the torus region. Outflow of the gas forms a hot ($T_g \sim 10^6$ K) funnel in the inner region. These structures and dynamics are energized by SNe with average SN rate of $\simeq 5.4 \times 10^{-5}$ yr^{-1}. Gas column densities toward the nucleus larger than 10^{22} cm^{-2}

are found if the viewing angle is smaller than $\theta_v \simeq 50^\circ$ from the edge-on. However, the column densities are distributed over almost 2 orders of magnitude around the average for any given viewing angle due to the clumpy nature of the torus. The column density of H_2 shows a similar distribution, and $N_{H_2} \gtrsim 10^{22}$ cm^{-2} is achieved for $\theta_v \lesssim 30^\circ$. For stronger FUV ($G_0 = 100$), the total H_2 mass in an equilibrium is only a little smaller ($\simeq$0.35) and the molecular gas is slightly more concentrated in a plane, while other properties of the ISM are also not very sensitive to the FUV intensity and SN rate. Vertical velocity dispersion of the gas in the torus ($\simeq$20 km s^{-1} on average) is enhanced only by a factor of $\sim$1.5 for increasing the SN rate by 2 orders of magnitude.

The structure and dynamics of these nuclear molecular disk presented here are very similar to molecular gas disk in various types of nearby AGNs recently revealed by rovibration line of H_2 using VLTI/SINFONI and Keck/OSIRIS (Hicks et al. 2009). The inconsistency on column density toward the center in NGC 1097 between the large column density suggested by CO observations (Hsieh et al. 2008) and X-ray (Terashima et al. 2002) could be attributed to the inhomogeneous structures emerging from the hereby presented disk models.

Finally, in the present results, it is notable that although the assumed FUV and SN rate may differ by orders of magnitude among the models, the total molecular gas fraction settles between $f_{H_2} \simeq 0.3$–0.4. This weak "negative" feedback from FUV and SNe on the star formation in the central region, suggests that substantial molecular gas disks can survive around AGNs with strong ongoing star formation.

We thank the anonymous referee for his/her valuable comments. We are also grateful to Nozomu Kawakatu and Masako Yamada for helpful discussions. The numerical computations presented in this paper were carried out on NEC SX-9 in the Center for Computational Astrophysics, NAOJ. This work is partly supported by a collaborating project between NAOJ and NEC.

APPENDIX A

NUMERICAL RECIPE OF H_2 FORMATION AND DESTRUCTION

Abundance of hydrogen molecule of each hydrodynamic grid-cell (0.125 or 0.25 pc) at a given time step is determined by the following time-dependent approach coupled with hydrodynamic equations. In this approach, H_2 and H I are assumed fully mixed within "cells" of typical radius R_c whose choice is motivated by the ISM physics, while it remains unresolved by the simulation during the course of the thermodynamic and dynamic evolution of the gas. This allows a smooth treatment of the H I–H_2 mass exchange in both the Cold Neutral Medium (CNM) and Warm Neutral Medium (WNM) phases, with all factors now incorporated in a single equation, namely

$$\begin{aligned}\frac{dn_2(\vec{r})}{dt} &= R_f(T_k)n(\vec{r})^2 \\ &- \left[2R_f(T_k)n(\vec{r}) + \frac{G_0 k_d}{4\pi}\int_{4\pi} f_s(N_2)e^{-\tau(\Omega)}d\Omega\right]n_2(\vec{r}) \\ &- \gamma_1(T_k)\left[n(\vec{r}) - 2n_2(\vec{r})\right]n_2(\vec{r}) - \gamma_2(T_k)n_2(\vec{r})^2. \quad \text{(A1)}\end{aligned}$$

The factor $k_d = 4 \times 10^{-11}$ s^{-1} is the unshielded FUV-induced H_2 dissociation rate, G_0 is the FUV radiation field in Habing units (1.6×10^{-3} ergs cm^{-2} s^{-1}), τ is the FUV optical depth, $n(\vec{r}) = n_1(\vec{r}) + 2n_2(\vec{r})$ (n_1: neutral hydrogen density, n_2: H_2 density), and $\gamma_1(T_k)$, $\gamma_2(T_k)$ are the H–H_2 and H_2–H_2 collisional destruction rates of H_2 for gas temperature T_k that can be fitted using data from Martin et al. (1998). The function $R_f(T_k)$ is the H_2 formation factor. We set $R_f = 3.5\,\mu \times 10^{-17}(T_k/100\text{ K})^{1/2}S_H(T_k)$ cm^3 s^{-1} (Jura 1975; Pelupessy et al. 2006) for $T_k \leqslant 500$ K, otherwise $R_f = 0$. The factor μ represents observational uncertainties in the H_2 formation rate, with the canonical value (Jura 1975) corresponding to $\mu = 1$, but values up to $\mu = 5$ are possible (see Papadopoulos et al. 2002). Here we adopt $\mu = 5$, since this seems more probable form ISO studies of Galactic PDRs (Papadopoulos et al. 2002, and references therein). The function $S_H(T_k)$ quantifies the sticking probability of an H atom on a grain, which we set to unity for most of the modeling done in this work (the H_2 formation probability after sticking is considered unity throughout). We only test the case of $S_H = (1 + T_k/T_\circ)^{-2}$, where $T_\circ = 100$ K which was obtained by Buch & Zhang (1991), and is thought to be good for dust grains in general, as long as they are covered by a few layers of weakly bonded material.

The $f_s(N_2)$ function denotes the H_2 self-shielding factor, with N_2 being the H_2 column density, and

$$\begin{aligned} f_s &= 1, && \text{for } N_2 \leqslant N_0 = 10^{14}\text{ cm}^{-2}, \\ &= \left(\frac{N_2}{N_0}\right)^{-k} && \text{for } N_2 > N_0, \quad \text{(A2)}\end{aligned}$$

where $k = 3/4$ (see Draine & Bertoldi (1996)).

If we integrate Equation (A1) over the volume ΔV_c of the cell, while assuming negligible dust absorption within it ($\tau(\Omega) \sim 0$) we obtain,

$$\begin{aligned}\frac{dn_2}{dt} &= R_f(T_k)n^2 - \left[2R_f(T_k)n + G_0 k_d\left(\frac{N_0}{n_2 R_c}\right)^k K(R_c)\right]n_2 \\ &- \gamma_1(T_k)(n - 2n_2)n_2 - \gamma_2(T_k)n_2^2, \quad \text{(A3)}\end{aligned}$$

where the factor $K(R_c)$ (R_c is a cloud radius) is

$$K(R_c) = \frac{1}{4\pi\,\Delta V_c}\int_{\Delta V_c}\int_{4\pi}\left(\frac{R_c}{|\vec{R}_c - \vec{r}|}\right)^k d\Omega d^3\vec{r} \quad \text{(A4)}$$

$$= \frac{3}{4-2k}\int_0^1 x\left[(1+x)^{-k+2} - (1-x)^{-k+2}\right]dx,$$

$$\text{where} \qquad x = r/R_c, \quad \text{(A5)}$$

$$= \frac{3 \times 2^{-k+3}}{(3-k)(4-2k)}\left[\frac{2(3-k)}{4-k} - 1\right], \quad \text{(A6)}$$

and for $k = 3/4$ results to $K(R_c) = 0.976$. Unlike Pelupessy et al. (2006), the description of the H I–H_2 gas mass exchange here does not involve the density-size power law. It utilizes only the much better established line-width-size scaling law found for molecular clouds (Heyer& Brunt 2004), and used here to define the "cell" size (Equation A7) within which H I and H_2 are assumed fully mixed. Aside from the much smoother implementation of the H_2 formation and destruction mechanisms that this allows, it yields a treatment that remains suitable for a gas phase that may not follow both scaling relations (i.e. diffuse and non self-gravitating gas).

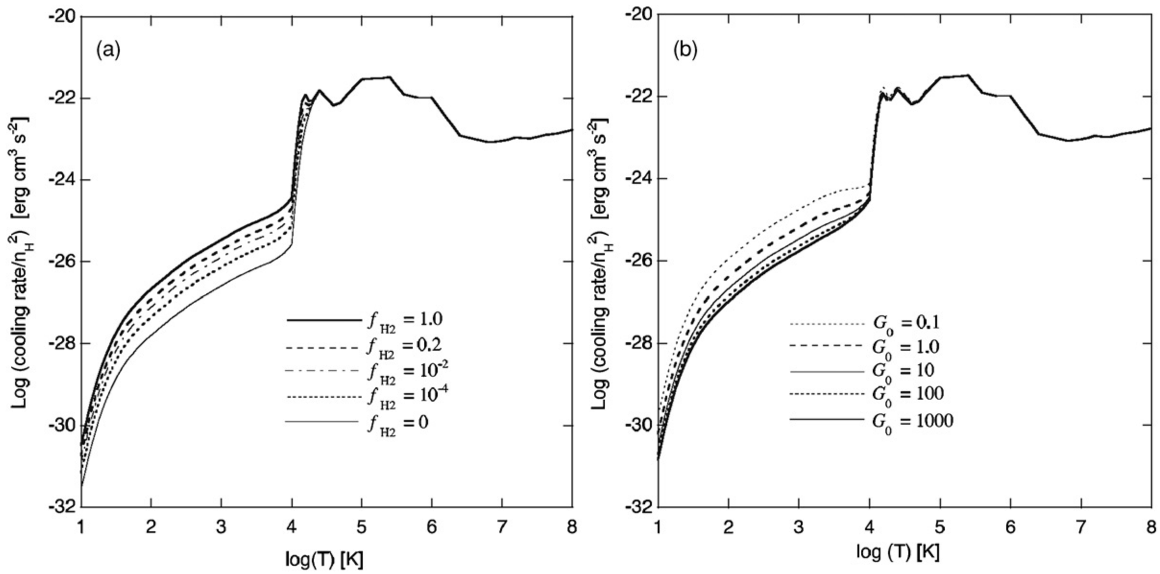

Figure A1. Cooling rate as a function of (a) f_{H_2} for $G_0 = 10$ and (b) G_0 for $f_{H_2} = 1.0$

The assumption of a typical H I–H_2 mixing subgrid "cell" where H_2 formation and dissociation takes places in full concomitance with H I greatly simplifies the problem of tracking the H I$\Leftrightarrow H_2$ gas phase exchange by reducing a non-local radiative transfer problem to a local one. Thus the H_2 fractions estimated are likely to be lower limits since H_2 self-shielding from FUV radiation occurring between distant "cells" (or dust absorption of the FUV radiation over scales larger than $2R_c$) can only result to higher H_2 fractions.

The local approximation made here in order to simplify a formidable radiative transfer problem in turbulent media still leaves the choice of the H I–H_2 mixing scale R_c open. A natural choice of R_c for our three dimensional hydrodynamic+thermodynamic ISM models would be $R_c \sim 1/2 l_p$, where l_p is the scale where the turbulent ISM pressure begins to dominate the thermal pressure, or equivalently the scale where the cloud size R_c-linewidth (ΔV) relation breaks down and $\Delta V(l_p) \sim \Delta V_{th}$. The corresponding radius is then given by:

$$R_c = 0.5 \left(\frac{\Delta V_{th}}{\Delta V_0}\right)^{1/q} \text{ pc},$$
$$\text{with} \quad \Delta V_{th} \simeq 0.8 (T_k/100\text{ K})^{1/2} \text{ km s}^{-1}, \tag{A7}$$

where $\Delta V(l) = \Delta V_0 (l/\text{pc})^q$ is the size-linewidth relation found for the cool ISM. Several observational and theoretical studies favor $q \sim 1/2$ (e.g., Larson 1981; Elmegreen 1989; Heyer& Brunt 2004). The normalization factor $\Delta V_0 = 1.2$ km s^{-1} for both CNM and WNM (Wolfire et al. 2003). Below such scales the thermal velocity fields take over, setting a natural resolution limit for any hydrodynamic ISM models tracking macroscopic gas motions. Moreover tracking the thermal state of the gas as a function of time and position allows R_c to adjust accordingly (cf. Equation (A7)), as expected in the true multiphase medium (e.g., Chieze & Pineau Des Forets 1987). Finally, by avoiding linking R_c to the numerical resolution of our hydrodynamic models (e.g., Glover & Mac Low 2007) keeps the computed H_2 gas mass fraction independent of it. We set a maximum value of R_c corresponding to the scale length of $T_k \sim 500$ K gas (cf. Equation (A7)). This temperature limit broadly marks the CNM→ WNM thermodynamic transition zone beyond which purely thermal motions fully overtake the macroscopic ones over the scales resolved here, while little H_2 content is expected ($R_f \sim 0$ for $T_k > 500$ K while collisional destruction of H_2 becomes very efficient).

In the case of CNM-to-WNM or the WNM gas phase, R_c can be substantial, and the dust extinction term can be important. Then we use

$$K(R_c) = \frac{1}{4\pi\, \Delta V_c} \int_{\Delta V_c} \int_{4\pi} \left(\frac{R_c}{|\vec{R}_c - \vec{r}|}\right)^k e^{-n\sigma_{\rm FUV}|\vec{R}_c - \vec{r}|} d\Omega d^3\vec{r}, \tag{A8}$$

which after some simplifications results to

$$K(R_c) = \frac{3}{2} \int_0^1 x \left[\int_{1-x}^{1+x} t^{1-k} e^{-(n\sigma_{\rm FUV} R_c)t} dt\right] dx,$$
$$\text{where} \quad x = r/R_c. \tag{A9}$$

The latter expression encompasses both dust extinction and H_2 self-shielding and is the correct one for use in Equation (A3). For $\sigma_{\rm FUV} = 0$, $K(R_c)$ becomes identical to that given in Equation (A6). In the case of pure dust shielding (i.e. $k = 0$), and after some calculations it becomes

$$K(R_c) = \frac{3}{2}\left[\frac{(2\alpha - 3) + (2\alpha^2 + 4\alpha + 3)e^{-2\alpha}}{\alpha^4}\right], \ \alpha = n\,\sigma_{\rm FUV} R_c. \tag{A10}$$

APPENDIX B

COOLING FUNCTION BASED ON PDR MODELS

The cooling curves (Figure A1) in temperature (T_g), H_2 abundance and radiation field strength G_0 are derived from a grid of PDR models that have a range in irradiation ($G_0 = 0$–10^4 values) and density 1–10^6 cm^{-3}. The radiation field extends beyond 13.6 eV according to a starburst99 spectrum for a Salpeter IMF, i.e., the H II region is computed as part of the PDR. The code of Meijerink & Spaans (2005), with the latest chemical rates and grain surface reactions as in Cazaux & Spaans (2009) is adopted.

The PDR models, for a given G_0 and density, are evaluated at the particular H_2 abundances and temperatures that they enjoy with depth to get a parameterization of the cooling rate in G_0, H_2

abundance and T_g. In general, the chemical and thermal balance in PDR models depends on the ambient density. As it turned out, a cooling curve extraction (density squared scaling) was possible because many cooling lines have critical densities well in excess of 10^3 cm^{-3}.

However, optical depth effects can suppress cooling and drive level populations to local thermodynamic equilibrium (LTE). Therefore, information on the typical column over which coolants exist chemically in a PDR are used to correct for line trapping, as follows. A local turbulent velocity dispersion (Gaussian σ) of $dV = 3$ km s^{-1} is adopted and some turbulent coherence length L (between 3 and 0.3 pc). This yields a formal velocity gradient dV/L for scales larger than L. If the opacity is concentrated on small physical scales, then radiation is trapped. Still, different parts of the PDR cloud do not see each other on large physical scales. In effect, one has an effective Sobolev approximation or not depending on the chemical stratification. We adopt $L = 0.3$ pc in these simulations to mimic the effects of a turbulently active nuclear region. In this, the multizone escape probability code of Poelman & Spaans (2005) is used for the radiative transfer in the cooling lines (under statistical equilibrium). Each zone in a PDR was treated this way, and a correction on the cooling curve due to line trapping effects can be derived.

For the warm and dense gas in the simulation clumps, the opacity is concentrated on small physical scales, leading to line trapping. For example, cooling lines like [C II] 158 μm, [O I] 63 μm and CO all have optical depths significantly larger than unity across a single PDR interface. Given that this PDR substructure is not resolved in the simulations, we feel that these opacity effect should be included.

The dust temperature is computed as part of the PDR model and is often larger than 30 K. The far-infrared radiation field produced by this dust is included in the statistical equilibrium of all cooling agents. Particularly water is quite sensitive to dust pumping and is an effective heater in the presence of dust grains warmer than 50 K.

At temperatures above 10^4 K the presence of an ionizing component in the impinging radiation field was found to suppress the cooling rate, compared to a collisionally ionized plasma, by a factor of ~3 for $T = 10^4$–10^5 K. This is of little concern in our hydrodynamical simulations. Line transfer in the resonantly scattered Lyman α line benefits very strongly from dust absorption and reradiation in the optically thin far-infrared continuum.

REFERENCES

Antonucci, R. 1993, ARA&A, 31, 473
Ballantyne, D. R. 2008, ApJ, 685, 787
Buch, V., & Zhang, Q. 1991, ApJ, 379, 647
Carollo, C. M., Stiavelli, M., Seigar, M., de Zeeuw, P. T., & Dejonghe, H. 2002, AJ, 123, 159
Cazaux, S., & Spaans, M. 2009, A&A, 496, 365
Cid Fernandes, R., Gu, Q., Melnick, J., Terlevich, E., Terlevich, R., Kunth, D., Rodrigues Lacerda, R., & Joguet, B. 2004, MNRAS, 355, 273
Chen, Y.-M., Wang, J.-M., Yan, C.-S., Hu, C., & Zhang, S. 2009, ApJ, 695, L130
Chieze, J.-P., & Pineau Des Forets, G. 1987, A&A, 183, 98
Collin, S., & Zahn, J.-P. 2008, A&A, 477, 419
Elmegreen, B. G. 1989, ApJ, 338, 178
Davies, R. I., Sánchez, F. M., Genzel, R., Tacconi, L. J., Hicks, E. K. S., Friedrich, S., & Sternberg, A. 2007, ApJ, 671, 1388
Draine, B. T., & Bertoldi, F. 1996, ApJ, 468, 269
Elitzur, M. 2008, New Astron. Rev., 52, 274
Fritz, J., Franceschini, A., & Hatziminaoglou, E. 2006, MNRAS, 366, 767
Glover, S. C. O., & Mac Low, M.-M. 2007, ApJ, 659, 1317
Heyer, M. H., & Brunt, C. M. 2004, ApJ, 615, L45
Hicks, E. K. S., Davies, R. I., Malkan, M. A., Genzel, R., Tacconi, L. J., Sánchez, F. M., & Sternberg, A. 2009, ApJ, 696, 448
Hockney, R. W., & Eastwood, J. W. 1981, Computer Simulation Using Particles (New York: McGraw Hill)
Hsieh, P.-Y., Matsushita, S., Lim, J., Kohno, K., & Sawada-Satoh, S. 2008, ApJ, 683, 70
Imanishi, M., Nakanishi, K., Tamura, Y., & Peng, C.-H. 2009, AJ, 137, 3581
Imanishi, M., & Wada, K. 2004, ApJ, 617, 214
Jaffe, W., et al. 2004, Nature, 429, 47
Jura, M. 1975, ApJ, 197, 581
Kawakatu, N., & Wada, K. 2008, ApJ, 681, 73
Kennicutt, R. 1998, ApJ, 498, 541
Kohno, K., Ishizuki, S., Matsushita, S., Vila-Vilaró, B., & Kawabe, R. 2003, PASJ, 55, L1
Krolik, J. H. 2007, ApJ, 661, 52
Larson, R. B. 1981, MNRAS, 194, 809
Levenson, N. A., Sirocky, M. M., Hao, L., Spoon, H. W. W., Marshall, J. A., Elitzur, M., & Houck, J. R. 2007, ApJ, 654, L45
Levenson, N. A., Weaver, K. A., & Heckman, T. M. 2001, ApJ, 550, 230
Liou, M., & Steffen, C. 1993, J. Comp. Phys., 107, 23
Maiolino, R., Shemmer, O., Imanishi, M., Netzer, H., Oliva, E., Lutz, D., & Sturm, E. 2007, A&A, 468, 979
Maloney, P. R., Hollenbach, D. J., & Tielens, A. G. G. M. 1996, ApJ, 466, 561
Martin, P. G., Keogh, W. J., & Mandy, M. E. 1998, ApJ, 499, 793
Meijerink, R., Spaans, M., & Israel, F. P. 2007, A&A, 461, 793
Meijerink, R., & Spaans, M. 2005, A&A, 436, 397
Meisenheimer, K., et al. 2007, A&A, 471, 453
Papadopoulos, P. P., Thi, W.-F., & Viti, S. 2002, ApJ, 579, 270
Pelupessy, F. I., Papadopoulos, P. P., & van der Werf, P. 2006, ApJ, 645, 1024
Pier, E. A., & Krolik, J. H. 1993, ApJ, 418, 673
Poelman, D. R., & Spaans, M. 2005, A&A, 440, 559
Poncelet, A., Perrin, G., & Sol, H. 2006, A&A, 450, 483
Riffel, R., Pastoriza, M. G., Rodríguez-Ardila, A., & Maraston, C. 2007, ApJ, 659, L103
Schartmann, M., Meisenheimer, K., Camenzind, M., Wolf, S., Tristram, K. R. W., & Henning, T. 2008, A&A, 482, 67
Schartmann, M., Meisenheimer, K., Klahr, H., Camenzind, M., Wolf, S., & Henning, T. 2009, MNRAS, 393, 759
Sofue, Y., Tutui, Y., Honma, M., Tomita, A., Takamiya, T., Koda, J., & Takeda, Y. 1999, ApJ, 523, 136
Spaans, M., & Meijerink, R. 2008, ApJ, 678, L5
Terashima, Y., Iyomoto, N., Ho, L. C., & Ptak, A. F. 2002, ApJS, 139, 1
Tielens, A. G. G. M. 2005, The Physics and Chemistry of the Interstellar Medium (Cambridge: Cambridge Univ. Press)
Tristram, K. R. W., et al. 2007, A&A, 474, 837
Tristram, K. R. W., et al. 2009, arXiv:0903.4892
Urry, C. M., & Padovani, P. 1995, PASP, 107, 803
Vollmer, B., & Beckert, T. 2003, A&A, 404, 21
Vollmer, B., Beckert, T., & Davies, R. I. 2008, A&A, 491, 441
Vollmer, B., Beckert, T., & Duschl, W. J. 2004, A&A, 413, 949
Wada, K. 2001, ApJ, 559, L41
Wada, K. 2008, ApJ, 675, 188
Wada, K., Meurer, G., & Norman, C. A. 2002, ApJ, 577, 197
Wada, K., & Norman, C. A. 2001, ApJ, 547, 172
Wada, K., & Norman, C. A. 2002, ApJ, 566, L21 (WN02)
Wada, K., & Tomisaka, K. 2005, ApJ, 619, 93
Watabe, Y., Kawakatu, N., & Imanishi, M. 2008, ApJ, 677, 895
Wolfire, M. G., McKee, C. F., Hollenbach, D., & Tielens, A. G. G. M. 2003, ApJ, 587, 278
Yamada, M., Wada, K., & Tomisaka, K. 2007, ApJ, 671, 73